Massive-vortex realization of a Bosonic Josephson Junction

Massive-vortex realization of a Bosonic Josephson Junction

Alice Bellettini [1,*] Andrea Richaud [2] and Vittorio Penna [1]
[1]*Department of Applied Science and Technology, Politecnico di Torino, 10129 Torino, Italy*
[2]*Departament de Física, Universitat Politècnica de Catalunya, Campus Nord B4-B5, E-08034 Barcelona, Spain*

(Received 24 July 2024; accepted 15 October 2024; published 25 November 2024)

We study the mass exchange between two rotating, quantum massive vortices in a two-component Bose-Einstein condensate. The vortices, in the majority component, exhibit a filled core, where the in-filling minority component undergoes a quantum tunneling effect. Remarkably, we observe that the two-vortex system features stable Josephson oscillations, as well as all the nonlinear phenomena, including the macroscopic quantum self-trapping, that characterize a Bosonic Josephson Junction. We propose an analytical model for describing the intervortex tunneling, obtained by implementing the coherent-state representation of the two-mode Bose-Hubbard model. This allows us to give the explicit expression of the model's parameters in terms of the physical macroscopic parameters of the two-vortex system. The comparison of the dynamical scenario predicted by the model with that emerging from the Gross–Pitaevskii equations is very good for sufficiently small atom numbers, while at larger atom numbers it grows less precise, presumably due to the partial exclusion of the many-body interactions from our model. The definition of an effective self-interaction parameter allows us to include the many-body effects, thus restoring a quite good agreement with the numerical results. Interestingly, the recognition of the bosonic Josephson dynamics paves the way to the investigation of new dynamical behaviors in multivortex configurations.

DOI: 10.1103/PhysRevResearch.6.043197

I. INTRODUCTION

The recent research in quantum vortices with filled core [1,2] has unveiled novel and interesting phenomena, such as the formation of stable giant vortices [3–5] or exotic vortex lattices [6–8], vortex collisions [5], vortex splitting [9], and a richer dynamics with respect to massless vortices which includes rotational states of asymmetric vortex pairs and multimode oscillatory behaviors supported by inertial effects [10–12]. The larger manipulability of quantum gases compared with liquid helium has also opened the path to superfluidity experiments in different trap geometries [13–15] and even topologies [16–20]. Dilute, ultracold quantum gases are in fact confined via optical potentials, where the pinning of a vortex to a desired position is also possible [21,22]. Such a framework enabled experimental realizations of different configurations of "massive vortices." These topological excitations are realized in superfluid mixtures and involve a quantum vortex in the major component of the mixture, whose core is filled by a mass-peak of the second component.

Quantum massive vortices can occur in the miscible [9,23] or immiscible [24–26] regimes of a mixture formed by two condensates [27–29]. The dynamics of such a binary mixture, well described by two coupled Gross–Pitaevskii equations (GPEs) within a mean-field picture, shows in fact the formation of vortices in the majority component denoted by "*a*," while the minority component "*b*" accumulates at the vortex cores. This is possible as the quantum vortices represent phase singularities characterized by the formation of a local density well at their cores [30,31]. With the introduction of a second, minority component, such as a second atomic species or the same species associated with a different hyperfine state, the density wells at the vortex sites acquire the function of effective external potentials. As a consequence, the confinement of the infilling component within the vortex cores is particularly favored if the two components are immiscible, which is in fact the case we restrict ourselves to in this paper.

The effects of the density peaks in the component *b*, playing the role of effective inertial masses, were described via a point-like picture of the massive vortices [10,32,33]. In this framework, the vortex dynamics is described by Lorenz-like equations and involves the motion of the vortices while excluding the time dependence of the masses occupying the vortex cores. In this paper we overcome this constraint and investigate vortex configurations where a mass exchange between the vortices can take place, caused by a tunneling effect.

The well-known Bose-Hubbard (BH) model describes the interwell tunneling effect of bosons that are trapped in arrays of potential wells. For this reason it provides the natural framework where the boson exchange between different vortex cores in a binary mixture can be realistically modeled.

The simplest possible model, the two-well BH model, has received outstanding attention in the last three decades both due to its integrable character and because its nonlinear dynamics, in addition to many interesting properties, exhibits a profound similarity with the Josephson-junction

*Contact author: alice.bellettini@polito.it

phenomenology. This aspect was emphasized by Milburn *et al.* [34] who conducted a study on the mean-field dynamics of neutral atoms of a Bose-Einstein condensate (BEC) in a double-well potential, highlighting the presence of regimes characterized by the self-trapping transition and the Josephson effect. Further studies of such system led to the definition of Bosonic Josephson Junction (BJJ) [35,36], and to the observation of the ac and dc Josephson effects [37].

The theoretical literature on BJJs is vast. Among many aspects and effects, it ranges from the coherent-state picture of BJJ dynamics [38], the study of the double-well dynamics with the GPE [39], the number squeezing effect [40] and exact multiconfigurational dynamical approaches [41], to phase diffusion processes [42], the transition to dissipative and self-trapping regimes [43] and the realization of atomtronics devices [44]. The effect of a second component on the Josephson oscillations [45] and on the spectral properties [46] were also explored for a binary condensate in a double-well potential or in more complex geometries [47–49].

On the experimental front, Ref. [50] reported the direct observation of oscillatory atomic currents in a chain of BJJs. However, the first realization of a single BJJ, with ^{87}Rb, was done by Albiez *et al.* [51] a few years later (a review on BJJ experiments is carried out in Ref. [52]). This validated the presence of tunneling oscillations and of the macroscopic quantum self-trapping, which was also observed in a one-dimensional periodic potential [53]. Afterwards, the creation of a BJJ with a binary condensate [54] allowed the dynamical effects due to the intraspecies interactions to be highlighted.

In this paper, we show that it is possible to realize a double-well BH model, namely, a BJJ, by means of a pair of two-dimensional (2D) quantum massive vortices occurring in the component a when the tunneling process of b between the vortex cores is taken into account. Note that the component a, hosting the vortices, acts as an effective potential for the component b. Our results are supported by the numerical simulation of the coupled GPEs for the mixture. Surprisingly, we find that the intervortex mass imbalance and phase-shift between the two peaks, as obtained from the GPEs dynamics, reproduce the BH phase portraits characterizing a double-well system, where the trajectories are both stable over time and robust against eventual b leaks outside of the vortex cores.

To validate these findings we implement the space-mode approximation of the field Hamiltonian of the component b and derive analytically the two-mode BH model and the relevant mean-field version within the coherent-state picture. This allows us to find the phase-space portrait of the BJJ, well known in the literature (see, e.g., Refs. [36,38]). The comparison of the mean-field model with the phase portrait provided by the GPE simulations shows a remarkably good agreement. Interestingly, this result implies that vortices can be used, in place of optical potentials, to support the formation of a BJJ. In passing, we note how the derivation of the two-mode BH Hamiltonian allows us to find analytical expressions for the interaction and tunneling *parameters* directly related to the macroscopic physical parameters of the vortex pair.

Pola *et al.* [55] already investigated the possibility of creating a BJJ via a vortex *dipole* hosting a solitonic component. In their work, however, they observed the BJJ dynamics in the limit of a frozen vortex dipole and of a very few atoms of the in-filling component. Conversely, in our paper, we prove the existence of a robust BJJ dynamics for long times and for a wide range of b-component atom numbers. In fact, the support of the BJJ is in our case a orbiting vortex pair, where the two vortex wells have the same circulation. Unlike in Ref. [55], our system, involving also large numbers of atoms in the vortex-hosting component, does not present a significant breathing of the vortices.

This paper is articulated as follows: In Sec. II we motivate our work and introduce the GPEs describing the mixture and the vortex pair dynamics. Following up on that, we present in Sec. III the numerical results revealing the presence of a Bosonic Josephson Junction in the system of the massive vortex pair, proving its stability and robustness. In Sec. IV we subsequently introduce the analytical framework connected to a Bosonic Josephson Junction, starting from a two-mode BH Hamiltonian and deriving then its mean-field version via the coherent-state variational approach. Here we also derive some explicit analytical expressions for the parameters of the Bose-Hubbard model in terms of the macroscopic parameters of the vortex-pair system. We then discuss the comparison of the numerics with the analytical model in Sec. V, and sum up the conclusions and outlooks in Sec. VI. Hereafter, for the sake of simplicity, we refer to the double-well or two-mode BH model with the term *BH dimer*.

II. GROSS–PITAEVSKII DYNAMICS AND BOSONIC JOSEPHSON JUNCTION REALIZATION

The current paper is prompted by Ref. [12] where we proved the existence of asymmetric rotational states of a vortex pair involving two mass-imbalanced vortices with the same circulation. The vortices rotate specularly around the origin at different radial positions. Our analytical solution relied on a point-like model, which is based on the time-dependent variational Lagrangian approach [10,56]. We characterized all the possible configurations of the vortex pair, obtaining a rich diagram of the rotational states, also involving massless vortices. Moreover, we discussed the dynamical stability of the solutions in the presence of small perturbations. Here arose the intuition that an adiabatic variation of the vortex masses could be a phenomenon present in GPE dynamics of the mixture. In this case, by switching to a suitable rotating frame of reference, a BJJ dynamics for the b component could be retrieved.

We consider here a symmetric vortex pair, where the two vortices are identical and specularly rotating at the same distance r_1 from the origin. The properties of the condensates' mixture are well captured by two coupled Gross–Pitaevskii equations [57], describing the two ultracold dilute quantum gases:

$$
\begin{aligned}
i\hbar\dot{\psi}_a &= \left(\frac{g_a}{L_z}|\psi_a|^2 + \frac{g_{ab}}{L_z}|\psi_b|^2 - \frac{\hbar^2\nabla^2}{2m_a} + V_{\text{ext}}\right)\psi_a, \\
i\hbar\dot{\psi}_b &= \left(\frac{g_b}{L_z}|\psi_b|^2 + \frac{g_{ab}}{L_z}|\psi_a|^2 - \frac{\hbar^2\nabla^2}{2m_b} + V_{\text{ext}}\right)\psi_b, \qquad (1)
\end{aligned}
$$

where $V_{\rm ext}(\boldsymbol{r})$ is the external potential, m_a and m_b are respectively the atomic masses of component a and component b, and g_a, g_b, and g_{ab} are the repulsive boson-boson interaction parameters, defined by

$$g_a = \frac{4\pi\hbar^2 a_a}{m_a}, \quad g_b = \frac{4\pi\hbar^2 a_b}{m_b}, \quad g_{ab} = \frac{2\pi\hbar^2 a_{ab}}{m_r},$$

where a_a and a_b are the intraspecies s-wave scattering lengths of components a and b, while a_{ab} is the scattering length between an atom of a and an atom of b. The reduced mass m_r is such that $1/m_r = 1/m_a + 1/m_b$. The interaction parameters in the Gross–Pitaevskii equations (1) are normalized by the parameter L_z, as a consequence of the reduction to two dimensions [58]. As a matter of fact, the modeling of a two-dimensional dynamics on the xy plane implies the presence of an effective thickness L_z in the direction z of the BECs layer, where the dynamics is frozen. The order parameters $\psi_a = \psi_a(x, y, t)$ and $\psi_b = \psi_b(x, y, t)$ are such that

$$\int d^2r|\psi_a|^2 = N_a, \quad \int d^2r|\psi_b|^2 = N_b,$$

where N_a and N_b are the number of atoms of component a and b, respectively, and represent two constant of motions.

For the numerical simulation of the GPEs we employ a mixture of ^{23}Na (a) and ^{39}K (b) confined in a two-dimensional (2D) disk of radius $R = 50$ μm. Hence, $V_{\rm ext}(\boldsymbol{r})$ is a rigid wall potential in correspondence of the disk boundary and zero inside the disk. The masses m_a and m_b are respectively the atomic masses of ^{23}Na and of ^{39}K. In the following, we always take $N_a = 10^5$ for the numerical simulations. The s-wave scattering lengths related to the repulsive interaction parameters are $a_a \simeq 52.0a_0$, $a_b \simeq 7.6a_0$, $a_{ab} \simeq 24.3a_0$, where a_0 is the Bohr radius. Note that, in our case, $g_{ab}/\sqrt{g_a g_b} = 1.26$, i.e., the two components are immiscible [59]. At higher values of this ratio, the density profile at the vortex sites shifts further from a local harmonic potential, whereas in the miscible regime the two peaks grow delocalized from the vortex centers. The effective thickness of the layer in the direction z is $L_z = 2 \times 10^{-6}$ m.

III. RESULTS

The numerical simulations of the two corotating massive vortices show, with unexpected clarity, that the intervortex mass exchange essentially reproduces the BJJ mechanism (see Appendix A for the code's description). The two vortices persistently orbit around the trap center keeping a constant distance (up to a small ripple of the order of $10^{-3}R$ that we neglect), and the local fraction of component b is well trapped although the a-density profile is only locally harmonic. This is visible in Fig. 1, showing the density profiles of both the components a and b.

Remarkably, both the linear region of the phase portrait as well as the nonlinear phenomena, such as the macroscopic quantum self-trapping, are captured. In Appendix B we recall the phase portraits' regimes of a standard Bosonic Josephson Junction and their fixed points. From the comparison of the numerical results with these plots, one can infer the positions of the fixed points (if not clearly visible). In our numerical results, we extract the (θ, D) trajectories, where θ is half

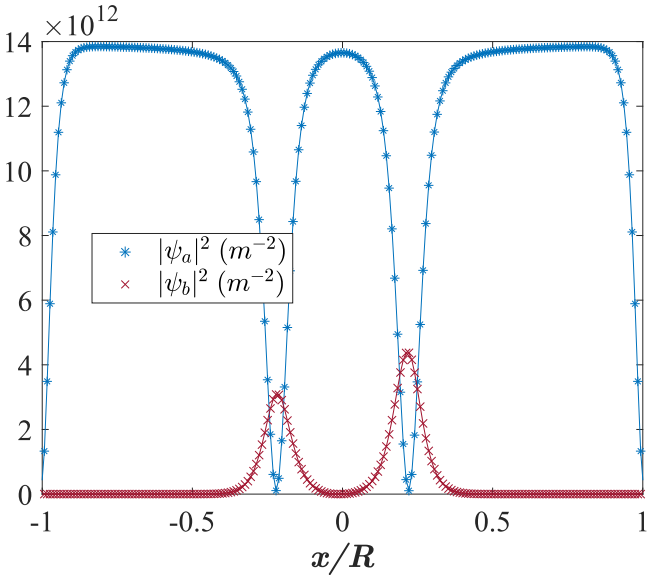

FIG. 1. Density profiles $|\psi_a|^2$ and $|\psi_b|^2$ at $t = 0$ along the x direction and at $y = 0$. The a component hosts a vortex pair while b is the tunneling component, featuring a BJJ dynamics. $N_b = 300$.

the b peaks' phase difference, $\theta = (\phi_1 - \phi_2)/2$, and D is the peaks' population imbalance, $D = N_1 - N_2$, $D \in [-N_b, N_b]$. The quantities ϕ_i and N_i are respectively the phase of peak i, numerically extracted as an average, and the number of b atoms in the peak i. Note that the quantity Dm_b gives the mass imbalance between the two peaks. The curves, corresponding to different initial conditions resemble the iso-energetic levels of the BJJ phase portrait. The examples in Figs. 2–6 show

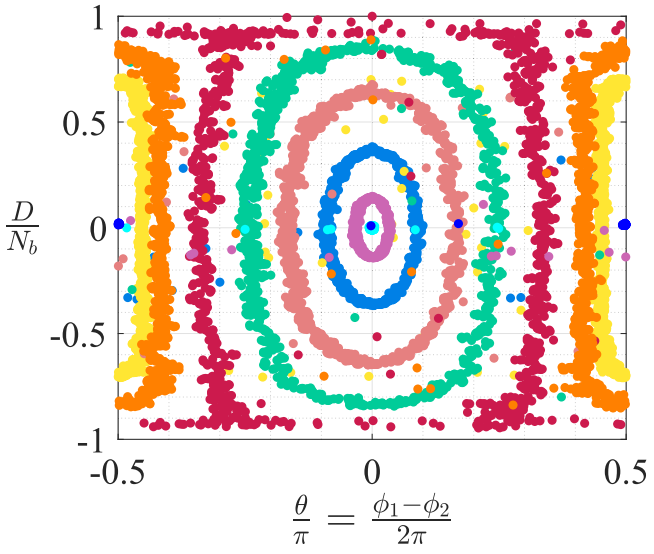

FIG. 2. GPE (θ, D) curves for a system with $N_b = 100$ and $r_1/R \simeq 0.22$. The collection of the extracted trajectories resembles the BH-dimer dynamics in a specific regime. The two fixed points of the BJJ model are reproduced along the axis $D = 0$. Whereas the trajectories corresponding to the Josephson oscillations run anticlockwise throughout the system's dynamics, the π oscillations run clockwise.

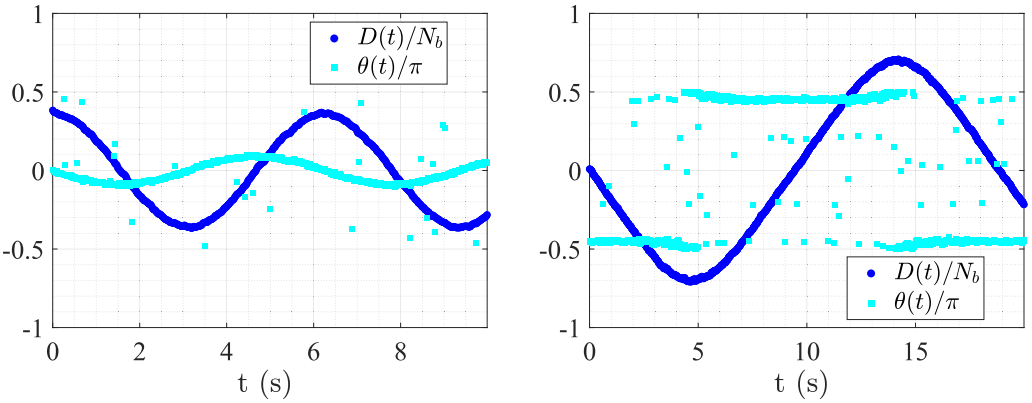

FIG. 3. Examples for the dynamical evolution of the conjugate variables D and θ for a trajectory in the Josephson oscillations region (left) and for a trajectory in the π oscillations region (right). The trajectories belong to the phase portrait in Fig. 2.

at a mean-field level that the corotating vortex pair makes up a Bosonic Josephson Junction. Here, the oscillations of the phase difference of the two local peaks are coupled with their mass imbalance. This phenomenon is possible thanks to the existence of circular orbit solutions for the vortex pair, that support a mass flux of the b component in the effective double-well potential given by the vortex wells. As mentioned, we interpret in the first place the two vortices as a time-independent potential, in a rotating frame of reference. In this way, the BH-dimer dynamics is effectively decoupled from the vortex pair dynamics.

More specifically, Figs. 2, 4, and 6 show examples of (θ, D) trajectories for different systems, corresponding to different structures of the phase space in the BH formalism (each trajectory in the phase space has a different color). Besides, in Fig. 3 examples of the time evolution of the conjugate variables are illustrated. For the data visualization in the figures, the phase-space variables D and θ are respectively normalized by the number of particles N_b and 2π. The characteristic BJJ trajectories are present, stable over time, and robust. The initial conditions on θ and D do not compromise the BJJ dynamics. Not only the characteristic Josephson and π oscillations are present but also, remarkably, the separatrices of such domains are well reproduced by the numerics. The method we employ for extracting θ is subject to small artifacts (outliers) that are, however, not of concern because we neglect them in the analysis of our results. Although we did not plot all the trajectories, the phase portraits are symmetric with respect to the origin so that the self-trapping can involve the large population of any of the two vortices. Note that the angle θ is naturally endowed with periodic boundary conditions, leading to the cylinder geometry of the phase space.

Figure 2 shows an example where both the Josephson (around the origin) and the π oscillations (around $|\theta| = 0.5\pi$) of the peaks' population imbalance D and their local phase difference θ are present. D and θ are extracted as described in Appendix A. One can see that the intervortex tunneling allows for Josephson oscillations of different amplitude around the

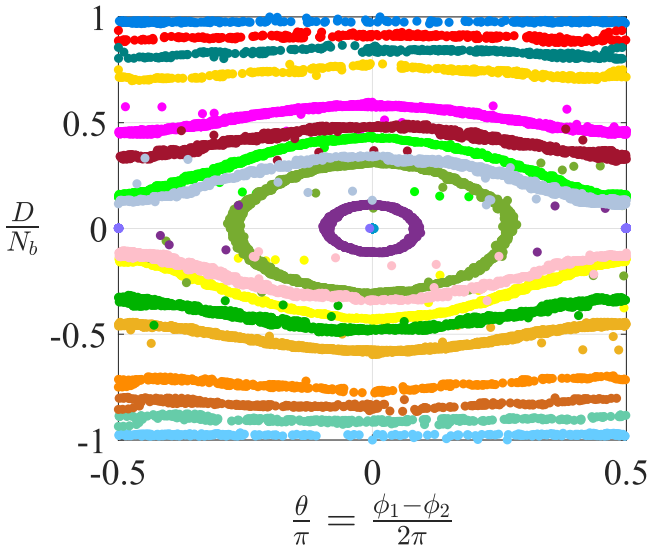

FIG. 4. GPE (θ, D) curves for a system with $N_b = 2000$ and $r_1/R \simeq 0.31$. Two fixed points of the BJJ model are simulated along the $D = 0$ axis. The travel direction of the trajectories is anticlockwise.

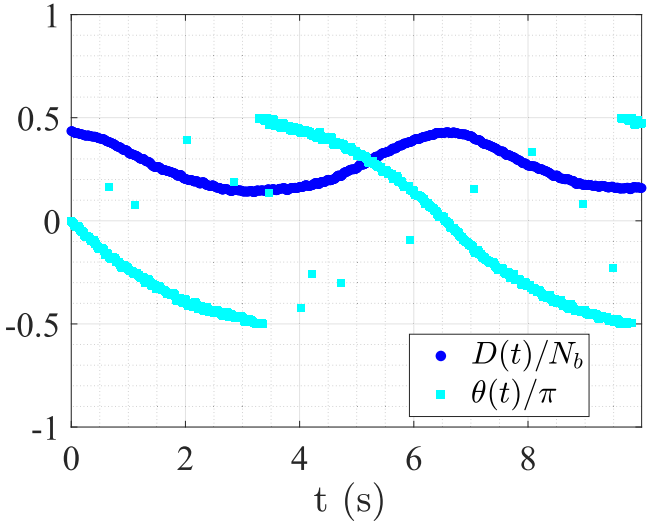

FIG. 5. Example of the time evolution of the BJJ's conjugate variables for a ballistic trajectory relative to the phase portrait in Fig. 4.

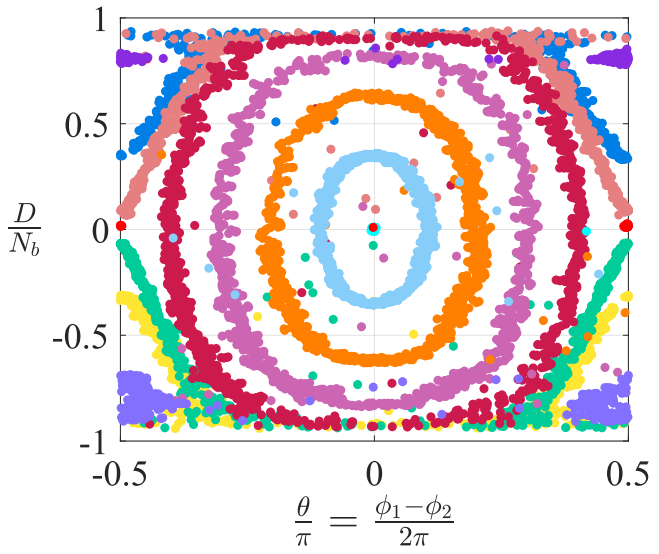

FIG. 6. GPE (θ, D) trajectories for a system with $N_b = 450$ and $r_1/R \simeq 0.22$. The numerics reproduce the four characteristic fixed points featured by a BJJ in this regime: two maxima, one saddle point, and one minimum. For the sake of illustration clarity we did not plot the symmetric counterpart, with respect to the origin, of the island-like trajectories at the corners of the phase space. These are traveled in clockwise direction during the BJJ dynamics, whereas the Josephson trajectories are run anticlockwise.

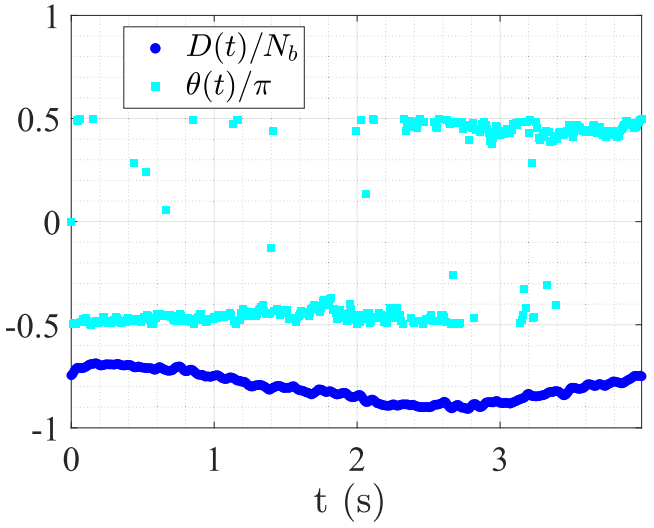

FIG. 7. Time evolution of D and θ for a self-trapped trajectory of the phase portrait in Fig. 6. In this example, the trajectory is the highly nonlinear regime, in the island-like region: both variables feature small oscillations around a nonzero average.

origin and that their frequency is smaller the larger they are. In the origin we see that a fixed point is reproduced by the GPE (the minimum of energy for a two-site BH model), while at large phase difference we see orbits characterized by large D variations, while $|\theta|$ is within some interval around 0.5π. In $|\theta| = 0.5\pi$ and $D = 0$, two other fixed points are correctly simulated. These correspond to maxima of the energy in a BH dimer. Around the separatrix between the domain including the origin and the higher $|\theta|$ domains, the numerical noise, as expected, increases. Remarkably, the ordered BH-dimer-like dynamics emerges as well in the highly nonlinear, far-from-the-origin, regions. Here, high values of the phase difference are involved, as well as large fluctuations of the mass imbalance. Also, note that, in the limit $D = \pm 1$, one of the two vortices has almost zero mass. Examples of the dynamics of the conjugate variables for the BJJ with the phase portrait of Fig. 2 are shown in Fig. 3. The dynamics illustrated in this figure is indicative of the variables' trend in the Josephson region, where both D and θ oscillate over time around a zero average, and in the π oscillations region. In the latter case, D features large oscillations around a zero average value, while the angular variable θ presents oscillations that have an extremely smaller amplitude, around the average value $-\pi/2$, coinciding with $\pi/2$.

The system in Fig. 4 represents a BJJ in another regime: here the on-site interactions are strong enough so to show self-trapping, i.e., the D oscillations around a mean value different from zero. In this case, these are coupled to the ballistic evolution of the phase difference. This is well visible in Fig. 5, where the phase shift time evolution is close to a linear relation, while the population imbalance features larger oscillations around a nonzero average. Such ballistic orbits are in fact characterized by large variations of θ, while $|D|$ stays confined around a mean value. Going back to Fig. 4, two fixed points of the BJJ model are clearly reproduced along the $D = 0$ axis: The minimum in the origin and the saddle point at $|\theta| = 0.5\pi$. The vortex pair contains here a larger number of atoms N_b and the vortex centers are more distanced with respect to the case of Fig. 2.

Finally, the BJJ of Fig. 6 features a regime where another type of π oscillations occurs around $|\theta| = 0.5\pi$. Such trajectories describe a case where one of the two corotating vortices has a large mass, while the other have a very small mass, so that the b population is always in its largest part trapped within a specific vortex. These π-oscillations regions, featuring also a self-trapping character, present large average values of D and occur at large average values of $|\theta|$, so that both quantities vary within a relatively small interval. They look like "islands" in the corners of the phase space, and the time evolution of the conjugate variables in this case is shown in the example in Fig. 7. Again in Fig. 6, the numerics reproduce the four characteristic fixed points featured by a BJJ in this regime: two maxima at large $|D|$ values and $|\theta| = 0.5\pi$ (note the periodic boundary conditions in θ), a saddle point in $|\theta| = 0.5\pi$ and $D = 0$, and the minimum in the origin.

We conclude this section discussing briefly a possible experimental implementation of our vortex-supported BJJ in a mixture of ^{23}Na and ^{39}K, trapped in a flat disk-trap via a digital micromirror device [14]. This specific mixture, experimentally realized in 2018 by Schulze *et al.* and by Castilho *et al.* in 2019 [60] features a relatively large tunability of the interactions. In particular, in Ref. [60], a compact and versatile setup for the nucleation of vortices in the ^{23}Na BEC was implemented, and a number of ^{23}Na condensed atoms of the order of 10^6 was produced. While the mentioned experiments are promising for the vortex nucleation in the mixture, the creation of massive vortices could be obtained via the experimental routine proposed in Ref. [5], where via a

component-selective potential, the minority component could be initially placed at the vortex nucleation positions. The vortices' nucleation at the desired positions is to be induced via phase-imprinting methods [61,62] or by stirring a laser beam [22,63–65], and eventually with the aid of a pinning potential [22]. Regarding the realization of the BJJ, as an example the experiments in Refs. [51,54] are promising instances for a possible observation of the BJJ dynamics in the minority component, as well as the experiments with Fermi superfluids of Refs. [66,67]. The latter give rise to the intriguing question on which kind of intervortex tunneling phenomena may arise in the context of Fermi superfluids.

IV. THEORETICAL MODELING: ESTIMATE OF THE BOSE-HUBBARD PARAMETERS

Given a circular-orbit solution [12], where the two vortices are rotating specularly to each other around the origin at frequency Ω, we can treat the vortex pair as an effective external potential for the component b. When switching to a rotating reference frame of frequency Ω, the effective external potential becomes virtually time-independent. Hence, the Hamiltonian relative to the component b, in the second quantization formalism, is

$$\mathcal{H} = \mathcal{H}_0 + \mathcal{U} = \mathcal{H}_0 + \int d^3r \frac{g_b}{2} (\hat{\psi}_b^+)^2 \hat{\psi}_b^2, \tag{2}$$

$$\mathcal{H}_0 = \int d^3r \left(-\frac{\hbar^2}{2m_b} \hat{\psi}_b^+ \Delta \hat{\psi}_b \right) + g_{ab} \int d^3r \rho_a \hat{\psi}_b^+ \hat{\psi}_b - \Omega \int d^3r \hat{\psi}_b^+ L_3 \hat{\psi}_b, \tag{3}$$

and L_3 is the z component of the angular momentum operator,

$$L_3 = -i\hbar \left(x \frac{\partial}{\partial y} - y \frac{\partial}{\partial x} \right). \tag{4}$$

In Appendix C 3, we show that, for two corotating vortices, the angular-momentum term in Hamiltonian (3) is zero. In the above, $\rho_a = \rho_a(\boldsymbol{r}) = |\psi_a(\boldsymbol{r})|^2$ is the density profile of the majority component a and all the spatial vectors are 2D. Note that the component a only contributes to $\mathcal{H}$ via the term $g_{ab}\rho_a$, which is the effective external potential felt by the component b and is treated as time-independent.

From the Gaussian ansatz in Eq. (6) [11] we derive the oscillation frequency ω of any of the wells in the locally harmonic potential approximation. As aforementioned, we consider here identical wells at distance r_1 from the origin. Hence, the two wells have the same Gaussian width σ_a:

$$\omega^2 = \frac{2g_{ab}n_a}{m_b \sigma_a^2 L_z}, \quad n_a = \frac{N_a}{\pi \left(R^2 - 2\sigma_a^2\right)}. \tag{5}$$

$$\rho_a = \frac{n_a}{L_z} \left(1 - \sum_{i=1}^{2} e^{-\frac{|\boldsymbol{r} - \boldsymbol{r}_{v,i}|^2}{\sigma_a^2}} \right), \tag{6}$$

where $\boldsymbol{r}_{v,i}$ is the 2D vector of coordinates of vortex i.

A. Space-mode approximation

Starting from the Hamiltonian (2), we perform a two-mode approximation in the spirit of Ref. [34]. We expand the field operator $\hat{\psi}_b$ in terms of space modes

$$\hat{\psi}_b = \sum_{i=1}^{2} \hat{b}_i(t) W_i(\boldsymbol{r}), \quad i = 1, 2, \tag{7}$$

where $\hat{b}_i$ are the bosonic mode operators, such that $[\hat{b}_i, \hat{b}_j] = [\hat{b}_i^+, \hat{b}_j^+] = 0$ and $[\hat{b}_i, \hat{b}_j^+] = \delta_{ij}$. The functions $W_i(\boldsymbol{r})$, in Eq. (7), are the ground-state wave functions of the right well "1" and of the left well "2" (corresponding to the two effective potential wells placed at the vortex cores in component a), in the local harmonic approximation of the well profiles,

$$V_{\text{har}} = \frac{1}{2} m_b \omega^2 |\boldsymbol{r} - \boldsymbol{r}_{v,i}|^2, \quad \omega^2 = g_{ab} \frac{2n_a}{m_b L_z \sigma_a^2}.$$

From now on the dependency of the mode operators on time and of W_i on space are left implicit. The functions W_i are given by

$$W_i = \gamma \exp(-\alpha |\boldsymbol{r} - \boldsymbol{r}_{v,i}|^2), \quad \alpha = \frac{m_b \omega}{2\hbar}, \tag{8}$$

with the normalization constant $\gamma = \sqrt{2\alpha/(\pi L_z)}$. Note that, at large values of $g_{ab}/\sqrt{g_a g_b}$, different functions W_i might be more appropriate to precisely capture the BJJ dynamics.

After plugging the ansatz described by Eq. (7) into the Hamiltonian (2), we obtain the final b Hamiltonian in the two-mode approximation (refer to Appendix C for its explicit derivation in the general case of two different vortex orbits),

$$\mathcal{H}_{tm} = \frac{U}{2} \sum_{i=1}^{2} \hat{n}_i(\hat{n}_i - 1) - \mu N_b - J(\hat{b}_2^+ \hat{b}_1 - \hat{b}_1^+ \hat{b}_2), \tag{9}$$

with $N_b = \sum_{i=1}^{2} \hat{n}_i$, $\hat{n}_i = \hat{b}_i^+ \hat{b}_i$ the particle number operator of site i, and

$$\mu = -\frac{g_{ab} n_a}{L_z (1 + 2\alpha\sigma_a^2)} \left(1 - 2\alpha\sigma_a^2 e^{-\frac{8\alpha r_1^2}{1 + 2\alpha\sigma_a^2}} \right), \tag{10}$$

the chemical potential. The contribution μN_b can be neglected as N_b, being a constant of motion, does not affect the properties of the system. The interaction and tunneling parameters,

$$U = \frac{g_b \alpha}{\pi L_z} = \frac{g_b}{\hbar \pi L_z} \sqrt{\frac{g_{ab} n_a m_b}{2\sigma_a^2 L_z}} \tag{11}$$

and

$$J = \frac{g_{ab} n_a}{L_z} \left[\frac{1}{\sigma_a^2} \left(\frac{\hbar}{m_b \omega} + r_1^2 \right) e^{-\frac{m_b \omega}{\hbar} r_1^2} + \frac{4}{2 + 1/(\alpha\sigma_a^2)} e^{-\frac{4\alpha r_1^2 (1 + \alpha\sigma_a^2)}{1 + 2\alpha\sigma_a^2}} \right], \tag{12}$$

respectively, are calculated for a double-well system corresponding to a vortex pair where the vortices are at the same distance from the disk center but in opposite positions ($\mathbf{r}_2 = -\mathbf{r}_1$). Note the dependency, in Eqs. (11) and (12), on the macroscopic vortex parameters. At increasing $g_{ab}n_a$ the harmonic-oscillator (squared) frequency ω^2 increases, leading in turn to a stronger confinement and hence to a rise in the onsite interaction U. Conversely, U decreases with increasing σ_a, i.e., the Gaussian vortex-profile width. Furthermore, U depends linearly on the b atoms interaction parameter g_b, as in

standard BH models, while the tunneling parameter J rapidly decreases with increasing r_1, i.e., the vortices' half-distance. It is also worth observing that the second term in Eq. (12) represents an extra contribution with respect to the standard tunneling parameter of Ref. [34]. This is due to the fact that the effective potential created by the vortices features a harmonic characteristic length $(2\alpha)^{-1/2}$ that is comparable with the vortex width σ_a (of the same order of the component-a healing length), and to σ_a being in general not negligible with respect to the vortices' distance $2r_1$.

In Appendix C we derive the general expression of J for the case where the two vortices rotate onto two different circumferences. We proved the existence of these configurations for two individual massive vortices in Ref. [12], and their extension to a BJJ is analogous to the single-orbit case.

Note that, according to Milburn, Corney *et al.* [34], the two-mode approximation is only valid in the limit

$$N_b \ll \sqrt{\frac{\hbar}{2m_b\omega}}\frac{1}{a_b} = N_h, \tag{13}$$

i.e., when the intraspecies interactions do not perturb significantly the ground state of the harmonic oscillators. Note as well that, as $N_h \propto 1/(a_b\sqrt[4]{g_{ab}})$, the smaller is the scattering length of a_b or the smaller is g_{ab}, the more the ansatz (7) is appropriate for capturing the double-well phenomenology

B. Mean-field approximation

Since the numbers of bosons contained in the two wells is rather large, the purely quantum description based on Hamiltonian (9) can be replaced by the mean-field BH model obtained within the coherent-state picture of Ref. [38]. The mean-field Hamiltonian is given by $\mathcal{H}_{\rm mf} = \langle\psi_b|\mathcal{H}_{tm}|\psi_b\rangle$, where $|\psi_b\rangle$ reads

$$|\psi_b\rangle = e^{i\frac{S}{\hbar}}|Z\rangle, \quad |Z\rangle = \otimes_{i=1,2}|z_i\rangle,$$

and S is the effective action related to Hamiltonian $H_{\rm mf}$. The state $|z_i\rangle$ is the Glauber coherent state whose parameter $z_i = \langle z_i|b_i|z_i\rangle \in \mathbb{C}$ represents the local order parameter of the well i and allows one to define the relevant average boson population $|z_i|^2 = \langle z_i|b_i^+ b_i|z_i\rangle$. The resulting mean-field Hamiltonian is

$$H_{\rm mf} = \sum_{j=1}^{2}\frac{U}{2}|z_j|^4 - J(z_2^* z_1 + z_1^* z_2),$$

whose derivation is discussed in Appendix D. With a convenient change of variables, the phase space is reduced to two dimensions. By defining the new pairs of canonically conjugate variables,

$$D = |z_1|^2 - |z_2|^2, \quad \theta = \frac{\phi_1 - \phi_2}{2},$$

$$\mathcal{N} = |z_1|^2 + |z_2|^2, \quad \psi = \frac{\phi_1 + \phi_2}{2},$$

where $z_j = |z_j|e^{i\phi_j}$, the following final BJJ Hamiltonian is obtained:

$$H_{\rm mf} = \frac{U}{4}\mathcal{N}^2 - \mu\mathcal{N} + \frac{U}{4}D^2 - J\sqrt{\mathcal{N}^2 - D^2}\cos(2\theta). \tag{14}$$

Note that the variable $\mathcal{N}$ is a constant of motion representing the total number of atoms N_b of the BJJ, and ψ is an auxiliary variable, so that the phase space is made up by the two conjugate variables D and θ, where D represents the population imbalance between the two wells, while θ represents their phase shift. The relevant equations of motion read (the associated Poisson brackets are given in Appendix D)

$$\hbar\dot{D} = 2J\sqrt{\mathcal{N}^2 - D^2}\sin(2\theta), \tag{15}$$

$$\hbar\dot{\theta} = -\frac{U}{2}D - \frac{JD}{\sqrt{\mathcal{N}^2 - D^2}}\cos(2\theta), \tag{16}$$

while $\dot{\mathcal{N}} = 0$ and the equation for ψ plays the role of an auxiliary equation. Again, following Ref. [38] it is convenient to define the quantity

$$\Gamma = \frac{2J}{U\mathcal{N}}, \tag{17}$$

discriminating different regimes of the phase portrait. Finally, the frequency ν of the (θ, D) orbits in the small-oscillation limit [i.e., close to (0,0)] is

$$\nu = \sqrt{\frac{2J\mathcal{N}U}{\hbar^2}\left(1 + \frac{2J}{\mathcal{N}U}\right)} = \frac{2J}{\hbar}\sqrt{\frac{1}{\Gamma}(1+\Gamma)}, \tag{18}$$

while a solution of Eqs. (15) and (16) in the linear domain is given by $D = A\cos(\nu t)$ and $\theta = -\frac{A\nu\hbar}{4J\mathcal{N}}\sin(\nu t)$ with A depending on the initial condition. The frequency ν (18) depends on the properties of the mixture and on the distance between the two vortices.

V. RESULTS AND DISCUSSION: COMPARISON WITH THE GROSS–PITAEVSKII EQUATION DYNAMICS

We compare the GPE results with the two-well mean-field BH model predictions using for the BH parameters the analytical expressions (11) and (12) in terms of the parameters of the vortex pair. We take a series of parameter pairs (U, J) while only N_b varies and we compare the GPE phase portraits and the real-time dynamics with the trajectories obtained via our model. Here, we set $\sigma_a = 0.179R$, $N_a = 10^5$, and $r_1 \simeq 0.22R$.

We find that, for a small number of atoms, i.e., $N_b = 10$, there is a general good agreement between the model and the GPE, both in the phase portrait and in the BH-dimer dynamics (see Figs. 8–10). As visible in Fig. 8, a mismatch only stems in the strongly nonlinear regime, characterized by π-phase oscillations [$\theta(t) \approx \pi/2$]. These are, however, still qualitatively captured. Focusing on the time evolution, Fig. 9 compares the GPE and BH dynamics in the Josephson oscillations domain [which features small oscillations of $D(t)$ and $\theta(t)$) around zero]. Here we see that not only the shape of the trajectories in the phase space is well captured but also the BH-dimer dynamics. When going further from the linear region, as in Fig. 10, we see that our model underestimates the frequency of BH-dimer dynamics, while the shape of the (θ, D) trajectory is still qualitatively well captured. In general, in the nonlinear region the ratio of the GPE-extracted frequency to the BH model frequency $\nu_{\rm GPE}/\nu_{\rm BH}$ can vary approximately from 1.1 to 1.6 for the tested trajectories. To sum up, in the small-N_b limit, the analytical expressions for the BH model parameters are reliable and the macroscopic effects occurring in the BJJ

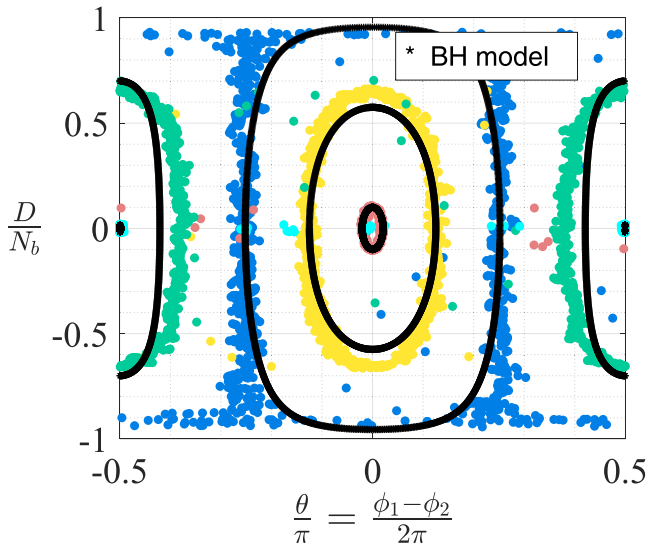

FIG. 8. Comparison between the GPE-extracted phase portrait and our analytical BH model. $N_b = 10$, $\Gamma \simeq 1.5$. Whereas the π oscillations' trajectories are traveled in a clockwise direction, the Josephson oscillations' trajectories are traveled anticlockwise.

are well described. However, for trajectories in the phase space that are further from the Josephson-oscillation domain, some small discrepancy arises. These involve situations of a larger mass-imbalance between the two vortices, which may excite other phenomena in the GPE simulation. In general, this suggests that this discrepancy is not of concern, rather, the good agreement still persisting is remarkable.

The larger N_b, the more evident the mismatch, which is, however, substantially improved via an effective correction of the coefficient U [Eq. (11)]. In this case, we obtain an overall good agreement of the phase portraits such as those in Figs. 11–13, where some nonqualitative discrepancies arise again only in the strongly nonlinear domain. This is the case in the π oscillations region of Fig. 11, and in the π-oscillations "islands" of Figs. 12 and 13. Regarding the time evolution of the conjugate variables for a BJJ at larger N_b, we find that the double-well dynamics is often well reproduced by the numerical simulations. The oscillation frequency in the evolution of D and θ can be underestimated by our model of a factor $\nu_{\rm GPE}/\nu_{\rm BH}$ that goes approximately from 1.1 to 1.6 for the examined trajectories. As an example, the time evolution of D and θ illustrated in Fig. 14 are cases of a very good agreement between the frequency of the BH- and the GPE-extracted dynamics at larger N_b values (in this case $N_b = 1000$) and upon the effective correction of U.

This effective correction of U is such that $U_{\rm eff} = U/f$, where $f > 1$ and in most cases f increases with N_b. The value of f is found via the best fit of the phase-space trajectories and variables' dynamics, as obtained via the GPEs with our model. We interpret this correction as an effective correction of g_b, namely, as an effect of the intraspecies interactions, which are not taken into account in the space-mode approximation. The ansatz (8) is in fact valid in the limit expressed by Eq. (13). Parameter g_b controls the repulsive interactions, resulting in a wider b peak with respect to the noninteracting case. Furthermore, this effect is larger for larger N_b, something that gives a reasonable interpretation of the U correction. Possible ways to improve the model include the numerical computation of the BH parameters, or models that go beyond the standard two-mode approximation [39,68].

Finally, we mention an alternative scheme that could be adopted to interpret the discrepancies. One could in fact always leave U untouched and tune the parameter σ_a for every system, at most to large effective values, so that the phase portrait provided by numerical simulations features a very good agreement with that of the double-well BH model. This, however, at the price of losing the agreement in the real-time dynamics, obtaining in fact a large overestimation of the frequency by the model, which increases with increasing N_b.

VI. CONCLUSIONS AND OUTLOOK

To sum up, the thorough numerical study of the dynamics of a massive-vortex pair unveiled a robust realization of the BJJ, triggered by the intervortex b-boson tunneling. We extracted several phase portraits from the simulation of the coupled Gross–Pitaevskii equations and observed, remarkably, all the characteristic phenomena featured by a BJJ, including the Josephson and π oscillations and the macroscopic quantum self-trapping. Thanks to the existence of

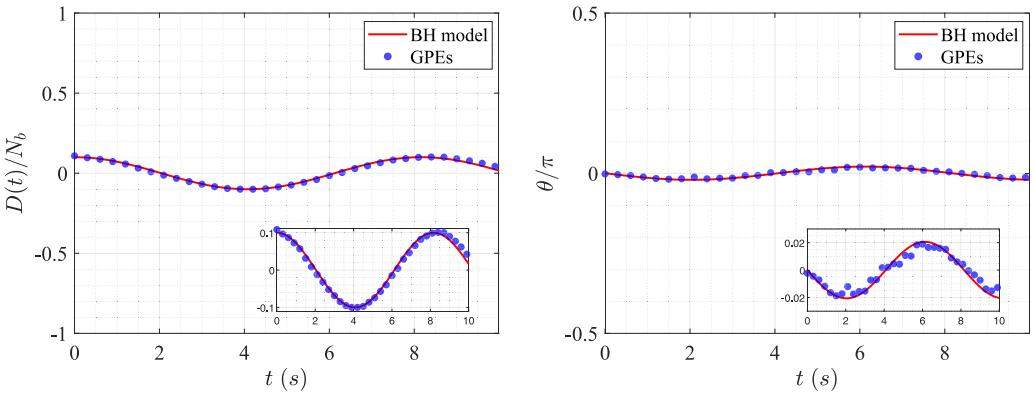

FIG. 9. Comparison between the time evolution of the population imbalance D (left) and the phase shift θ (right) as extracted from the GPEs versus as predicted by our analytical model, for a trajectory close to the origin in the phase space, i.e., in the linear domain (zoom in the insets). The system is the same of Fig. 8, with $N_b = 10$.

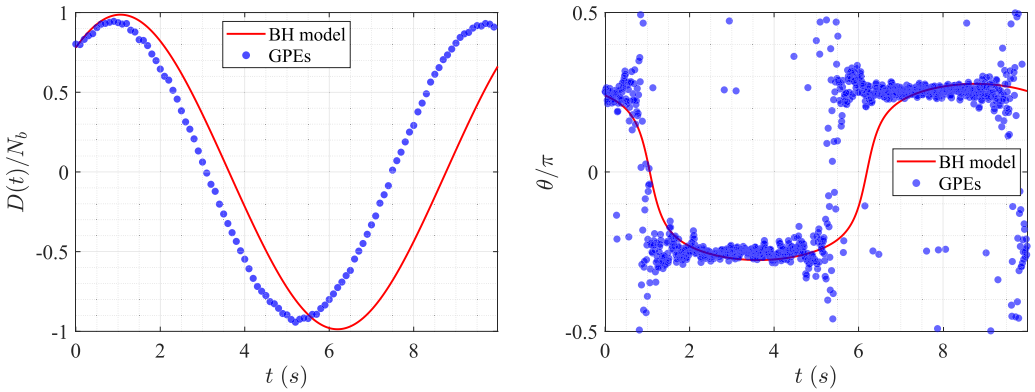

FIG. 10. (left) Comparison between the dynamics of D as extracted from the GPEs versus the results of our analytical model, for a large orbit at the boundary with the π-oscillation domain, i.e., a trajectory in the strongly nonlinear domain. (right) Comparison between the dynamics of the phase shift θ as extracted from the GPE versus the prediction of our analytical model for the same trajectory as the left panel. The system is the same as in Fig. 8, with $N_b = 10$.

circular orbit solutions for the two vortices [12], we were able to treat the vortex pair as fixed-point solution in a rotating frame of reference. Thus, they constitute a time-independent effective potential for their in-filling component, tunneling within the two-vortex effective double-well potential. Despite the small, fast variations of the vortex radial positions, the BH-dimer dynamics stayed unaffected and stable over time. Hence, vortices in BECs can be used in replacement to optical potentials to support the formation of a BJJ. The remarkable fact that vortices can host a component undergoing quantum tunneling offers a rich and intriguing scenario. This suggests future extensions starting from the minimum building block, i.e., the vortex pair, here presented.

We modeled the BJJ Hamiltonian associated with the component b filling the two vortex cores. In our system, ψ_a represents a background time-independent order parameter. Starting from the quantum b Hamiltonian, we performed a two-mode approximation and then derived, via a coherent-state approach, its corresponding mean-field version. We presented a final Bose-Hubbard model where the parameters are explicitly expressed in terms of the system's physical quantities. In the derivations, we considered b as localized around the center of two locally harmonic wells, a condition justified by the immiscibility of the two species.

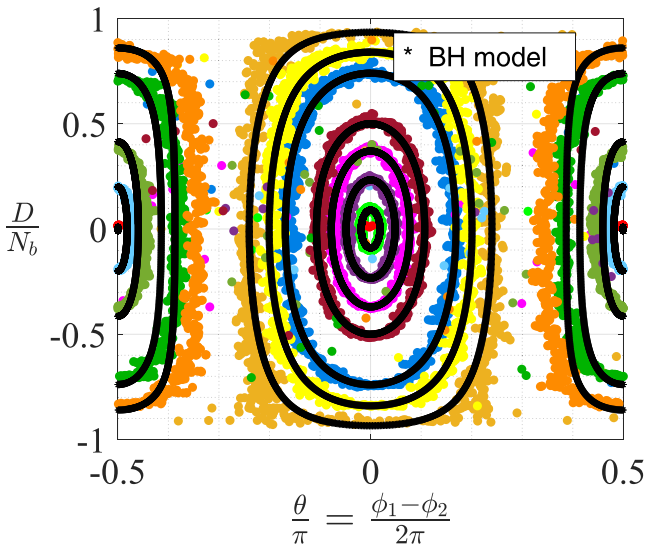

FIG. 11. Comparison between the GPE-extracted phase portrait and our analytical BH model. $N_b = 50$, $U_{\text{eff}} = U/5$, $\Gamma \simeq 1.5$. The Josephson oscillations' trajectories are traveled anticlockwise, while the π oscillations' trajectories are traveled clockwise during the BJJ dynamics.

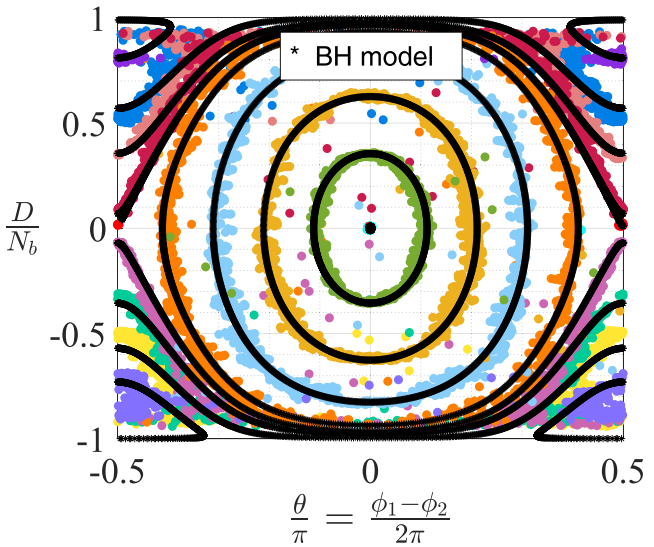

FIG. 12. Comparison between the GPE-extracted phase portrait and our analytical BH model. $N_b = 450$, $U_{\text{eff}} = U/11$, $\Gamma \simeq 0.4$. For illustrative purposes we did not plot for all the trajectories their symmetric counterpart with respect to the origin. This is the case for the self-trapped regimes in the corners of the phase space, where the trajectories are constrained within small ranges of both the conjugate variables and have nonzero average. The travel direction of the trajectories is as in Fig. 6.

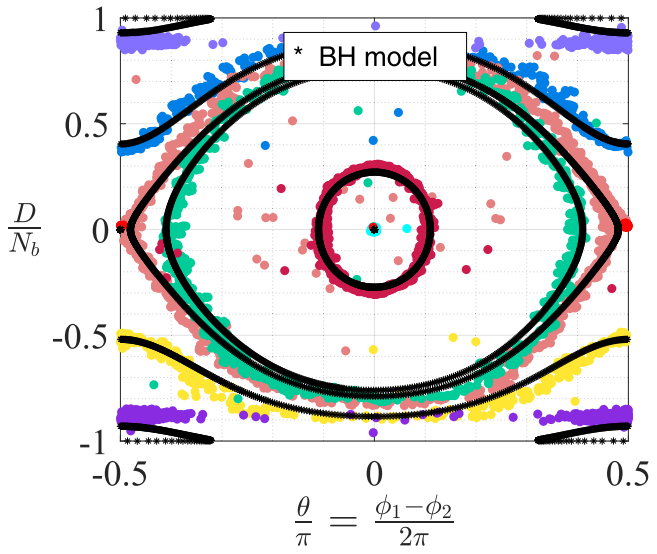

FIG. 13. Comparison between the GPE-extracted phase portrait and our analytical BH model. $N_b = 1000, U_{\text{eff}} = U/13, \Gamma \simeq 0.2$. The travel direction of the trajectories is anticlockwise, except for the π-oscillations "islands" at the corners of the phase portrait, where the direction is clockwise.

Finally, we compared our analytic Bose-Hubbard model with the numerical results. We found a very good agreement of the model with the GPE in the small-N_b limit, both in the phase portraits and in the BH-dimer dynamics, while at larger b-atom numbers an effective correction of the onsite interaction parameter U is necessary to obtain a good agreement with the numerics. We interpreted this correction, increasing with N_b, as an effect of the intraspecies interactions, which lead to an enlargements of the in-filling for the two-mode approximation. Nonetheless, an eventual improvement of the model via a new ansatz for the modes W_i is out of the scope of our paper, whereas it would be interesting for the future. Noticeably, the effectively corrected model was shown to capture even the separatrices in the phase portraits and the strongly nonlinear phenomena qualitatively. Some quantitative discrepancies can arise in the nonlinear regions, where the BH-dimer frequency is underestimated of up to a factor 1.6 for in the examined orbits. This is likely due to other phenomena occurring in the GPE, such as a more pronounced asymmetry in the vortex wells or larger variations of the vortex radial positions. As a future outlook, it would be in fact intriguing to incorporate into the model the coupling between the vortex dynamics and that of the BH-dimer, by taking into account the variations in the distance of vortices.

Other following-up scenarios include the vortex BH trimer and the emergence of chaos [49,69,70], the tunneling within a massive vortex necklace [71,72], and a lattice [73]. In addition, it would be interesting to model the asymmetric BH dimer [52,74], where the two vortices have different sizes. This is made possible thank to the in-filling component influencing the healing length of the condensate a. Further interesting outlooks are the inclusion of multiply quantized vortices, whose stability is guaranteed by the in-filling component [5], the case of attractive interactions [54], and the tunneling of a BEC mixture [47,48].

ACKNOWLEDGMENTS

A.R. received funding from the European Union's Horizon research and innovation programme under the Marie Skłodowska-Curie grant agreement *Vortexons* (Grant No. 101062887). A.R. further acknowledges support by the Spanish Ministerio de Ciencia e Innovación (MCIN/AEI/10.13039/501100011033, Grants PID2020-113565GB-C21 and PID2023-147469NB-C21), and by the Generalitat de Catalunya (Grant No. 2021 SGR 01411). Computational resources were provided by HPC@POLITO [75].

APPENDIX A: NUMERICAL SIMULATION

After nucleating the vortices via the imaginary-time procedure, we start the "real-time" simulation. Here the dynamics of the two order parameters is simulated by resolving the GPEs through the fourth-order Runge-Kutta algorithm. We compute the two vortex masses by integrating the b-density field ρ_b over two separated domains. These are obtained by dividing the disk domain (containing the mixture) by the axis of the segment through the two vortex centers. This method requires an initial estimate of the vortex positions, which is done via an image processing tool. Finally, we compute the phases of b peaks by integrating the b-phase field, weighted by ρ_b, onto separate domains that are further restricted in comparison with those employed for the masses. We restrict the data, in this case, to the neighborhoods of the two peaks, setting to zero all the data outside the circles of radius $0.01R$ centered in the two peaks. This is done to minimize numerical artifacts. Note that the distance between the two vortices should be large enough for a meaningful extraction of the vortex masses and phases as described above.

APPENDIX B: PHASE PORTRAITS OF A BOSONIC JOSEPHSON JUNCTION

In Fig. 15 we recall the different regimes of the phase portraits of a standard Bosonic Josephson Junction (see also Ref. [38]). The trajectories in the phase-space feature constant energy, and are relative to the Hamiltonian (14), with $N = \mathcal{N}$. The phase space is made up by the two conjugate variables D and θ, where D is the population imbalance between the two sites of the BJJ, and θ is half the phase difference between the two many-body states of the BJJ in the semiclassical approximation. In Fig. 15, $D \in [-N, N]$ is normalized by the number of particles N in the BJJ. Note that the phase portraits are symmetric with respect to the origin, and the phase space has a cylindrical geometry, due to the periodicity in θ featured by the Hamiltonian. The fixed points are sketched in red, and the labels "(m)," "(M)," and "(s)" indicate respectively an energy's local minimum, maximum, and saddle point. The parameter Γ (17) discriminates what regime the BJJ belongs to. Following the examples in the figure, from left to right and top to bottom, we can distinguish four different notable cases. (i) In the case of $\Gamma < 1/2$, the Josephson oscillations' orbits are present around the origin, while the ballistic trajectories are present in the nonlinear regime. These are instances of self-trapping and feature a free evolution of θ, while the population imbalance D stayed trapped around nonzero average values. An instance of π oscillations occurs at the corners of

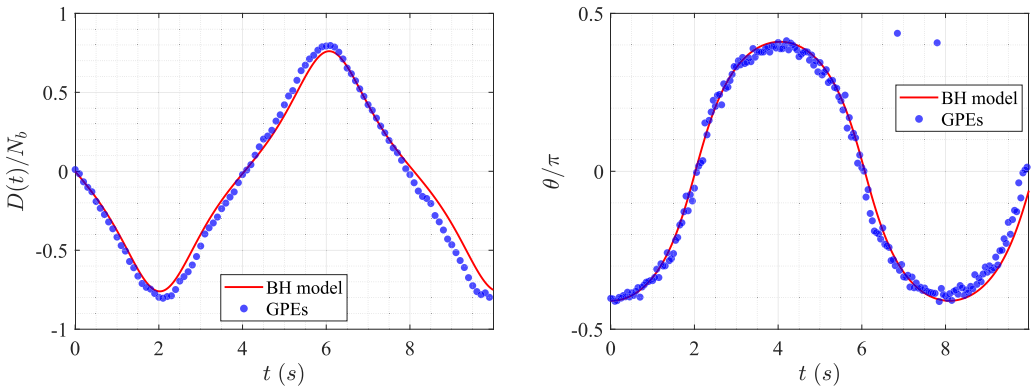

FIG. 14. (left) Comparison between the time evolution of the population imbalance D as extracted from the GPE and as predicted by our analytical model, for a trajectory close to the separatrix, in the phase space, between the Josephson oscillations region and the ballistic phase shift oscillations. (right) Comparison between the time evolution of the phase shift θ as extracted from the GPE and as predicted by our analytical model, for the same trajectory as in the left panel. The system is the same as in Fig. 13, $N_b = 1000$, $U_{\text{eff}} = U/13$.

the phase space, where island-like orbits take place. These also exhibit a self-trapping character. In these regions, both the conjugate variables vary over time with a nonzero average value. Four fixed points are present, i.e., the energy minimum in the origin, two energy maxima in the corners, and a saddle point at $(\theta = \pm 0.5\pi, D = 0)$. (ii) As Γ reaches the value of $1/2$, the ballistic orbits disappear, and the π-oscillations island-like regions expand in the vertical direction. As in the previous case, four fixed points are present. (iii) Further on, at $1/2 < \Gamma < 1$, a new type of π-oscillations orbits appears, featuring large oscillations of D, while $|\theta|$ is trapped around the average value of $\pi/2$. In this case, qualitatively, the same

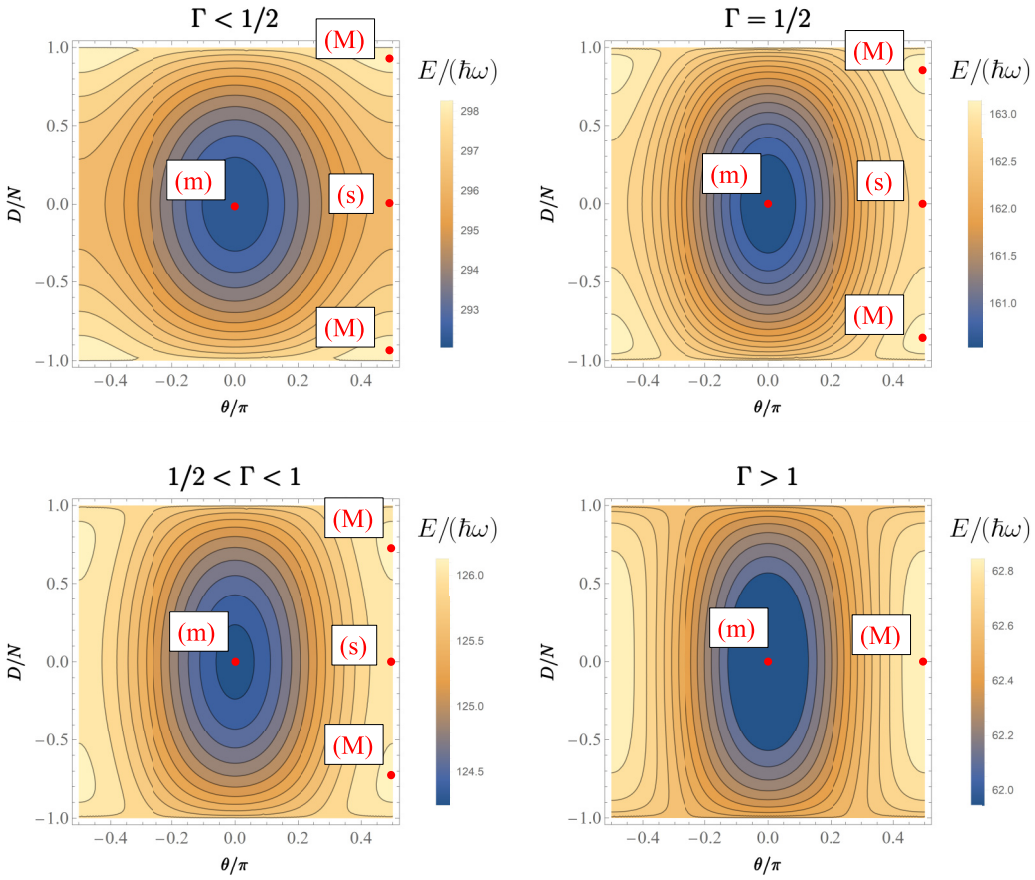

FIG. 15. Different regimes of the phase portraits of a BJJ. From left to right and top to bottom: $\Gamma \simeq 0.28$, $\Gamma = 0.50$, $\Gamma \simeq 0.65$, $\Gamma \simeq 1.30$. The colors represent the energy landscape of the BJJ, where the energy E given by the Hamiltonian (14) is normalized by $\hbar\omega$, with ω given by Eq. (5). The fixed points are sketched in red. Note that, due to the cylindrical geometry of the phase space, the fixed points can be equivalently represented on the straight line $\theta = 0.5\pi$ (as in the figure) or on the straight line $\theta = -0.5\pi$.

fixed points as in the previously examined regimes are present. (iv) Finally, at $\Gamma > 1$, the BJJ features no self-trapping regions, and only the Josephson and the π oscillations persist. In this final case, the two maxima have collapsed to the position ($\theta = \pm 0.5\pi, D = 0$), and the saddle point has disappeared. On the other hand, the position of the energy minimum in the origin persists.

APPENDIX C: SPACE-MODE APPROXIMATION

Here we present the derivation of the BH Hamiltonian in the general case of two vortices rotating on different orbits of radii r_1 and r_2, always with an angular position shift of π. Recall that we assume the vortex cores can be associated with a Gaussian width of σ_a, so that their corresponding potential wells have a frequency ω, in the harmonic approximation, given by

$$\omega^2 = \frac{2g_{ab}n_a}{m_b\sigma_a^2 L_z}.$$

Within the space-mode approximation the ground state of the ith well associated with the boson mode b_i is $W_i = \gamma e^{-\alpha|\boldsymbol{r}-\boldsymbol{r}_{v,i}|^2}$, with $\alpha = m_b\omega/2\hbar$ and $\gamma = \sqrt{2\alpha/(\pi L_z)}$, and we assume $(W_i, W_j) = \delta_{ij}$. In fact, we assume $\sigma_a \ll R$ and, justified by the immiscibility condition, $R^2 \gg 1/2\alpha$. Hence, the a-density profile at the vortex sites and the W_i wave functions are "narrow Gaussians." The Gaussian W_i is centered in the ith vortex position $\boldsymbol{r}_{v,i}$.

1. Free Hamiltonian $\mathcal{H}_0$

In the rotating reference frame the Hamiltonian $\mathcal{H} = \mathcal{H}_0 + \mathcal{U}$ of the component b exhibits two contributions. The second one $\mathcal{U}$ describes boson-boson interaction and will be analyzed later. The first one is

$$\mathcal{H}_0 = \int d^3r\left(-\frac{\hbar^2}{2m_b}\hat{\psi}_b^+\Delta\hat{\psi}_b\right) + g_{ab}\int d^3r\,\rho_a(\mathbf{r})\hat{\psi}_b^+\hat{\psi}_b - \Omega\int d^3r\,\hat{\psi}_b^+ L_3\hat{\psi}_b = (I) + (II),$$

where

$$\rho_a(\mathbf{r}) = \frac{n_a}{L_z}\left(1 - \sum_{i=1}^{2} e^{-\frac{|\boldsymbol{r}-\boldsymbol{r}_{v,i}|^2}{\sigma_{a,i}^2}}\right)$$

shows the g_{ab}-dependent coupling with the component-a density and the angular-momentum term emerging from the rotation. In the following we substitute the ansatz (7) into $\mathcal{H}_0$ and solve the integrals.

2. Integral (I)

$$(I) = \int d^3r\left(-\frac{\hbar^2}{2m_b}\hat{\psi}_b^+\Delta\hat{\psi}_b\right) + g_{ab}\int d^3r\,\rho_a\hat{\psi}_b^+\hat{\psi}_b = \sum_{i,j=1}^{2}\hat{b}_i^+\hat{b}_j\int d^3r W_i\left[H_{ho} + g_{ab}\rho_a - \frac{m_b\omega^2}{2}|\boldsymbol{r}-\boldsymbol{r}_{v,j}|^2\right]W_j = \sum_{i=1}^{2}\hat{b}_i^+\hat{b}_i E_0 + \sum_{j,i=1}^{2}\hat{b}_i^+\hat{b}_j K_{ij},$$

where the ground-state energy

$$E_0 = \frac{\hbar\omega}{2}$$

emerges from the action of the harmonic-oscillator (local) Hamiltonian

$$H_{ho} = -\frac{\hbar^2}{2m_b}\Delta + \frac{m_b\omega^2}{2}|\boldsymbol{r}-\boldsymbol{r}_{v,j}|^2$$

on its ground state W_j, and the two-index symbol K_{ij} reads

$$K_{ij} = \int d^3r W_i\left[g_{ab}\rho_a - \frac{m_b\omega^2}{2}|\boldsymbol{r}-\boldsymbol{r}_{v,j}|^2\right]W_j.$$

Hence, we can rewrite (I) as

$$(I) = \sum_{i=1}^{2}(E_0 + K_{ii})\hat{b}_i^+\hat{b}_i + \hat{b}_2^+\hat{b}_1 K_{2,1} + \hat{b}_1^+\hat{b}_2 K_{2,1} = \sum_{i=1}^{2}E_i\hat{n}_i + \hat{b}_2^+\hat{b}_1 K_{2,1} + \hat{b}_1^+\hat{b}_2 K_{2,1}.$$

After some long but not complex derivations, we obtain

$$K_{ij} = g_{ab}\frac{n_a}{L_z}\delta_{ij}^2 - \frac{\pi\gamma^2 g_{ab}n_a}{2\alpha + \frac{1}{\sigma_a^2}}\sum_{l=1}^{2}e^{A_\ell(x_i,x_j)}e^{A_\ell(y_i,y_j)} - \frac{\gamma^2}{2}m_b\omega^2 L_z e^{-\frac{\alpha}{2}|\boldsymbol{r}_{v,j}-\boldsymbol{r}_{v,i}|^2}\frac{\pi}{4\alpha}\left(\frac{1}{\alpha} + \frac{|\boldsymbol{r}_{v,j}-\boldsymbol{r}_{v,i}|^2}{2}\right), \tag{C1}$$

where $\boldsymbol{r}_{v,i} = (x_i, y_i)$,

$$A_\ell(x_i, x_j) = \exp\left[\frac{\left(\alpha X_{ij} + \frac{x_l}{\sigma_a^2}\right)^2}{2\alpha + \frac{1}{\sigma_a^2}} - \alpha\left(x_i^2 + x_j^2\right) - \frac{x_l^2}{\sigma_a^2}\right],$$

$X_{ij} = x_i + x_j$, and $A_\ell(y_i, y_j)$ is found by replacing x_i (x_j) with y_i (y_j) in A_ℓ. With the substitution $x_1 = r_1\cos\Theta$, $y_1 = r_1\sin\Theta$, $x_2 = -r_2\cos\Theta$, $y_2 = -r_2\sin\Theta$, i.e., taking two corotating vortices in the general case of two different orbits [12], we get, for $i \neq j$,

$$K_{ij} = -\frac{g_{ab}n_a}{L_z}\left[\frac{4}{2 + 1/(\alpha\sigma_a^2)}e^{-\frac{\alpha(1+\alpha\sigma_a^2)(r_1+r_2)^2}{1+2\alpha\sigma_a^2}} + \frac{e^{-\frac{\alpha}{2}(r_1+r_2)^2}}{2\sigma_a^2}\left(\frac{1}{\alpha} + \frac{(r_1+r_2)^2}{2}\right)\right]. \tag{C2}$$

Finally, for K_{ii} we obtain, for two corotating vortices

$$K_{ii} = \frac{g_{ab}n_a}{L_z\left(1 + 2\alpha\sigma_a^2\right)}\left(1 - 2\alpha\sigma_a^2 e^{-\frac{2\alpha(r_1+r_2)^2}{1+2\alpha\sigma_a^2}}\right) - \frac{\hbar\omega}{2}. \tag{C3}$$

3. Integral (*II*) (angular momentum)

We then substitute the ansatz (7) in the integral (*II*) and after doing some derivations we find

$$\begin{aligned}(II) &= -\Omega \int d^3r \hat{\psi}_b^+ L_3 \hat{\psi}_b \\ &= i\hbar\Omega \int d^3r \sum_{i=1}^{2} \hat{b}_i^+ W_i (x\partial_y - y\partial_x) \sum_{j=1}^{2} \hat{b}_j W_j \\ &= -2i\hbar\Omega L_z \sum_{i=1}^{2}\sum_{j=1}^{2} \frac{\gamma^2}{2} \hat{b}_i^+ \hat{b}_j e^{-\frac{\alpha}{2}(r_{v,i}^2 + r_{v,j}^2) + \alpha \boldsymbol{r}_{v,i}\cdot\boldsymbol{r}_{v,j}} \\ &\quad \times \left[-\frac{x_{v,i}+x_{v,j}}{2}\pi y_{v,j} + \frac{y_{v,i}+y_{v,j}}{2}\pi x_{v,j} \right].\end{aligned}$$

For two corotating vortices such that $x_1 = r_1\cos\Theta$, $y_1 = r_1\sin\Theta$, $x_2 = -r_2\cos\Theta$, $y_2 = -r_2\sin\Theta$, the factor in the square brackets is zero and $\mathcal{H}_0$ is rotation-invariant:

$$\left[-\frac{x_{v,i}+x_{v,j}}{2}\pi y_{v,j} + \frac{y_{v,i}+y_{v,j}}{2}\pi x_{v,j} \right] = 0.$$

4. Interaction term $\mathcal{U}$

Let us compute the interaction term $\mathcal{U}$ by substituting the ansatz (7) in the relevant expression:

$$\begin{aligned}\mathcal{U} &= \int d^3r \frac{g_b}{2} (\hat{\psi}_b^+)^2 \hat{\psi}_b^2 \\ &= \frac{g_b}{2} \int d^3r \sum_{i=1}^{2} \hat{b}_i^+ W_i \sum_{j=1}^{2} \hat{b}_j^+ W_j \sum_{k=1}^{2} \hat{b}_k W_k \sum_{l=1}^{2} \hat{b}_l W_l \\ &\simeq \frac{g_b}{2} \sum_{i=1}^{2} \int d^3r W_i^4 (\hat{b}_i^+)^2 \hat{b}_i^2 = \frac{g_b}{2} \sum_{i=1}^{2} K_0 \hat{n}_i(\hat{n}_i - 1),\end{aligned}$$

where

$$K_0 = \int d^3r W_i^4 = \frac{\alpha}{\pi L_z}.$$

Finally, the Hamiltonian $\mathcal{H}_0$ becomes, in the two-mode approximation,

$$\mathcal{H}_{tm} = -\mu \sum_{i=1}^{2} \hat{n}_i - J(\hat{b}_2^+ \hat{b}_1 - \hat{b}_1^+ \hat{b}_2) + \frac{U}{2} \sum_{i=1}^{2} \hat{n}_i(\hat{n}_i - 1), \tag{C4}$$

where $J = -|K_{12}| = -|K_{21}|$, $U = g_b K_0$, and $\mu = -(E_0 + K_{ii})$. In the limit $r_2 = r_1$, we obtain the parameters of Eqs. (10), (11), and (12).

APPENDIX D: MEAN-FIELD APPROXIMATION

The procedure of Ref. [38] for obtaining the mean-field Hamiltonian associated with $\mathcal{H}_{tm}$ assumes that bosons in the ith well are described by the (local) coherent state $|z_i\rangle$, defined by the equation $b_i|z_i\rangle = z_i|z_i\rangle$, related to the annihilation operator $\hat{b}_i$ of the Weyl-Heisenberg algebra $\{b_i, b_i^+, b_i^+ b_i, \mathbb{I}_i\}$ at site i. The expectation values

$$\langle z_i|\hat{b}_i|z_i\rangle = z_i, \quad \langle z_i|\hat{n}_i|z_i\rangle = |z_i|^2,$$

show that z_i can be seen as the order parameter describing the phase order at the i-th site, while $\langle z_i|\hat{n}_i|z_i\rangle$ describes the average boson population. The trial state of the variational coherent-state approach for the many-boson component b can be written as

$$|\psi_b\rangle = e^{i\frac{S}{\hbar}}|Z\rangle, \quad |Z\rangle = \otimes_{i=1,2}|z_i\rangle,$$

where

$$|z_i\rangle = e^{-\frac{|z_i|^2}{2}} \sum_{m=0}^{+\infty} \frac{z_i^m}{\sqrt{m!}}|m\rangle, \quad z_i \in \mathbb{C},$$

and $|m\rangle$ are the eigenstates of the number operator $b_i^+ b_i$. By imposing the condition $\langle\psi_b|(i\hbar\partial_\tau - \mathcal{H}_{tm})|\psi_b\rangle = 0$ one gets the effective action

$$S = \int_0^t d\tau L, \quad L = i\hbar\langle Z|\partial_\tau|Z\rangle - \langle Z|\mathcal{H}_{tm}|Z\rangle,$$

where L represents the effective Lagrangian, and $H_{\rm mf} = \langle Z|\mathcal{H}_{tm}|Z\rangle$, corresponds to the effective Hamiltonian. After some derivations we find

$$\begin{aligned}H_{\rm mf} = \langle Z|\mathcal{H}_{tm}|Z\rangle &= \sum_{j=1}^{2} \left(\frac{U}{2}|z_j|^4 - \mu|z_j|^2 \right) \\ &\quad - J(z_2^* z_1 + z_1^* z_2).\end{aligned} \tag{D1}$$

The associated Euler-Lagrange equations are

$$i\hbar\dot{z}_1 = -\mu z_1 + U|z_1|^2 z_1 - J z_2, \tag{D2}$$

$$i\hbar\dot{z}_2 = -\mu z_2 + U|z_2|^2 z_2 - J z_1, \tag{D3}$$

while variables z_1^*, z_2^* obey the complex-conjugate version of these equations. Interestingly, the same equations of motion can be derived by defining the Poisson brackets

$$\{A, B\} = \frac{1}{i\hbar} \sum_{m=1}^{2} \left[\frac{\partial A}{\partial z_m}\frac{\partial B}{\partial z_m^*} - \frac{\partial A}{\partial z_m^*}\frac{\partial B}{\partial z_m} \right],$$

showing how brackets $\{z_i, z_k^*\} = \delta_{ik}/(i\hbar)$ replace commutators $\{b_i, b_k^+\} = \delta_{ik}$ in the derivation of the mean-field (semiclassical) picture of the BH dimer. Not surprisingly, the atoms' number $\mathcal{N} = \langle Z|\sum_i b_i^+ b_i|Z\rangle = |z_1|^2 + |z_2|^2$ represents a constant of motion, namely, $\{\mathcal{N}, \mathcal{H}_{\rm mf}\} = 0$. Via an appropriate transformation, we find two new pairs of canonical variables replacing z_1, z_1^*, z_2, z_2^*. These are

$$\mathcal{N} = |z_1|^2 + |z_2|^2, \quad \psi = \frac{\phi_1 + \phi_2}{2},$$

$$D = |z_1|^2 - |z_2|^2, \quad \theta = \frac{\phi_1 - \phi_2}{2},$$

where $z_j = |z_j|e^{i\phi_j}$ has been used. Finally, the mean-field Hamiltonian in the new variable reads

$$H_{\rm mf} = \frac{U}{4}\mathcal{N}^2 - \mu\mathcal{N} + \frac{U}{4}D^2 - J\sqrt{\mathcal{N}^2 - D^2}\cos(2\theta), \tag{D4}$$

associated with the Poisson brackets

$$\{A, B\} = \frac{1}{\hbar}\left[\frac{\partial A}{\partial D}\frac{\partial B}{\partial \theta} + \frac{\partial A}{\partial \mathcal{N}}\frac{\partial B}{\partial \psi} - \frac{\partial A}{\partial \theta}\frac{\partial B}{\partial D} - \frac{\partial A}{\partial \psi}\frac{\partial B}{\partial \mathcal{N}}\right],$$

satisfying $\{\theta, \mathcal{N}\} = 0 = \{\psi, D\}$, $\{\theta, D\} = -\frac{1}{\hbar} = \{\psi, \mathcal{N}\}$. The relative equations of motion

$$\hbar\dot{D} = 2J\sqrt{\mathcal{N}^2 - D^2}\sin(2\theta), \tag{D5}$$

$$\hbar\dot{\theta} = -\frac{U}{2}D - \frac{JD}{\sqrt{\mathcal{N}^2 - D^2}}\cos(2\theta), \tag{D6}$$

$$\hbar\dot{\mathcal{N}} = 0, \tag{D7}$$

$$\hbar\dot{\psi} = -\frac{U}{2}\mathcal{N} + \mu + \frac{J\mathcal{N}}{\sqrt{\mathcal{N}^2 - D^2}}\cos(2\theta), \tag{D8}$$

feature the conserved quantity $\mathcal{N}$, corresponding to N_b, and show that the variable ψ is auxiliary. Hence, the system is represented by the restricted phase space of the conjugate variables (θ, D), representing the phase shift of the two peaks and the population imbalance between the sites of the BJJ. Note that the coherent state approach holds if the local boson population $\langle\hat{n}_i\rangle$ is large enough. The expectation values

$$\hat{n}_i \approx \langle\hat{n}_i\rangle = \langle\hat{b}_i^+\hat{b}_i\rangle = |z_i|^2,$$
$$\hat{b}_i \approx \langle\hat{b}_i\rangle = z_i,$$
$$\hat{b}_i^+ \approx \langle\hat{b}_i^+\rangle = z_i^*$$

show how the coherent-state variational approach is equivalent to applying the Bogoliubov approximation.

[1] M. R. Matthews, B. P. Anderson, P. C. Haljan, D. S. Hall, C. E. Wieman, and E. A. Cornell, Vortices in a Bose-Einstein condensate, Phys. Rev. Lett. **83**, 2498 (1999).

[2] B. P. Anderson, P. C. Haljan, C. E. Wieman, and E. A. Cornell, Vortex precession in Bose-Einstein condensates: Observations with filled and empty cores, Phys. Rev. Lett. **85**, 2857 (2000).

[3] P. Kuopanportti, N. V. Orlova, and M. V. Milošević, Ground-state multiquantum vortices in rotating two-species superfluids, Phys. Rev. A **91**, 043605 (2015).

[4] S. Patrick, A. Gupta, R. Gregory, and C. F. Barenghi, Stability of quantized vortices in two-component condensates, Phys. Rev. Res. **5**, 033201 (2023).

[5] A. Richaud, G. Lamporesi, M. Capone, and A. Recati, Mass-driven vortex collisions in flat superfluids, Phys. Rev. A **107**, 053317 (2023).

[6] E. J. Mueller and T.-L. Ho, Two-component Bose-Einstein condensates with a large number of vortices, Phys. Rev. Lett. **88**, 180403 (2002).

[7] V. Schweikhard, I. Coddington, P. Engels, S. Tung, and E. A. Cornell, Vortex-lattice dynamics in rotating spinor Bose-Einstein condensates, Phys. Rev. Lett. **93**, 210403 (2004).

[8] P. Kuopanportti, J. A. M. Huhtamäki, and M. Möttönen, Exotic vortex lattices in two-species Bose-Einstein condensates, Phys. Rev. A **85**, 043613 (2012).

[9] P. Kuopanportti, S. Bandyopadhyay, A. Roy, and D. Angom, Splitting of singly and doubly quantized composite vortices in two-component Bose-Einstein condensates, Phys. Rev. A **100**, 033615 (2019).

[10] A. Richaud, V. Penna, R. Mayol, and M. Guilleumas, Vortices with massive cores in a binary mixture of Bose-Einstein condensates, Phys. Rev. A **101**, 013630 (2020).

[11] A. Bellettini, A. Richaud, and V. Penna, Relative dynamics of quantum vortices and massive cores in binary BECs, Eur. Phys. J. Plus **138**, 676 (2023).

[12] A. Bellettini, A. Richaud, and V. Penna, Rotational states of an asymmetric vortex pair with mass imbalance in binary condensates, Phys. Rev. A **109**, 053301 (2024).

[13] M. White, H. Gao, M. Pasienski, and B. DeMarco, Bose-Einstein condensates in rf-dressed adiabatic potentials, Phys. Rev. A **74**, 023616 (2006).

[14] N. Navon, R. P. Smith, and Z. Hadzibabic, Quantum gases in optical boxes, Nat. Phys. **17**, 1334 (2021).

[15] M. Caldara, A. Richaud, M. Capone, and P. Massignan, Massive superfluid vortices and vortex necklaces on a planar annulus, SciPost Phys. **15**, 057 (2023).

[16] N. Lundblad, R. A. Carollo, C. Lannert, M. J. Gold, X. Jiang, D. Paseltiner, N. Sergay, and D. C. Aveline, Shell potentials for microgravity Bose–Einstein condensates, npj Microgravity **5**, 30 (2019).

[17] Y. Guo, E. M. Gutierrez, D. Rey, T. Badr, A. Perrin, L. Longchambon, V. S. Bagnato, H. Perrin, and R. Dubessy, Expansion of a quantum gas in a shell trap, New J. Phys. **24**, 093040 (2022).

[18] A. Wolf, P. Boegel, M. Meister, A. Balaž, N. Gaaloul, and M. A. Efremov, Shell-shaped Bose-Einstein condensates based on dual-species mixtures, Phys. Rev. A **106**, 013309 (2022).

[19] N. S. Móller, F. E. A. dos Santos, V. S. Bagnato, and A. Pelster, Bose–Einstein condensation on curved manifolds, New J. Phys. **22**, 063059 (2020).

[20] M. A. Caracanhas, P. Massignan, and A. L. Fetter, Superfluid vortex dynamics on an ellipsoid and other surfaces of revolution, Phys. Rev. A **105**, 023307 (2022).

[21] M. C. Davis, R. Carretero-González, Z. Shi, K. J. H. Law, P. G. Kevrekidis, and B. P. Anderson, Manipulation of vortices by localized impurities in Bose-Einstein condensates, Phys. Rev. A **80**, 023604 (2009).

[22] E. C. Samson, K. E. Wilson, Z. L. Newman, and B. P. Anderson, Deterministic creation, pinning, and manipulation of quantized vortices in a Bose-Einstein condensate, Phys. Rev. A **93**, 023603 (2016).

[23] A. Gallemí, L. P. Pitaevskii, S. Stringari, and A. Recati, Magnetic defects in an imbalanced mixture of two Bose-Einstein condensates, Phys. Rev. A **97**, 063615 (2018).

[24] S. A. McGee and M. J. Holland, Rotational dynamics of vortices in confined Bose-Einstein condensates, Phys. Rev. A **63**, 043608 (2001).

[25] K. J. H. Law, P. G. Kevrekidis, and L. S. Tuckerman, Stable vortex–bright-soliton structures in two-component Bose-Einstein condensates, Phys. Rev. Lett. **105**, 160405 (2010).

[26] J. D'Ambroise, W. Wang, C. Ticknor, R. Carretero-González, and P. G. Kevrekidis, Stability and dynamics of massive

vortices in two-component Bose-Einstein condensates, arXiv:2407.10324.

[27] A. Burchianti, C. D'Errico, S. Rosi, A. Simoni, M. Modugno, C. Fort, and F. Minardi, Dual-species Bose-Einstein condensate of ^{41}K and ^{87}Rb in a hybrid trap, Phys. Rev. A **98**, 063616 (2018).

[28] T. A. Schulze, T. Hartmann, K. K. Voges, M. W. Gempel, E. Tiemann, A. Zenesini, and S. Ospelkaus, Feshbach spectroscopy and dual-species Bose-Einstein condensation of ^{23}Na - ^{39}K mixtures, Phys. Rev. A **97**, 023623 (2018).

[29] L. Cavicchioli, C. Fort, M. Modugno, F. Minardi, and A. Burchianti, Dipole dynamics of an interacting bosonic mixture, Phys. Rev. Res. **4**, 043068 (2022).

[30] L. Onsager, Statistical hydrodynamics, Nuovo Cimento **6**, 279 (1949).

[31] W. Fiszdon, Quantized vortices in helium II, J. Fluid Mech. **233**, 691 (1991).

[32] A. Richaud, V. Penna, and A. L. Fetter, Dynamics of massive point vortices in a binary mixture of Bose-Einstein condensates, Phys. Rev. A **103**, 023311 (2021).

[33] A. Kanjo and H. Takeuchi, A universal description of massive point vortices in superfluids, arXiv:2409.12808 (2024).

[34] G. J. Milburn, J. Corney, E. M. Wright, and D. F. Walls, Quantum dynamics of an atomic Bose-Einstein condensate in a double-well potential, Phys. Rev. A **55**, 4318 (1997).

[35] A. Smerzi, S. Fantoni, S. Giovanazzi, and S. R. Shenoy, Quantum coherent atomic tunneling between two trapped Bose-Einstein condensates, Phys. Rev. Lett. **79**, 4950 (1997).

[36] S. Raghavan, A. Smerzi, S. Fantoni, and S. R. Shenoy, Coherent oscillations between two weakly coupled Bose-Einstein condensates: Josephson effects, π oscillations, and macroscopic quantum self-trapping, Phys. Rev. A **59**, 620 (1999).

[37] S. Giovanazzi, A. Smerzi, and S. Fantoni, Josephson effects in dilute Bose-Einstein condensates, Phys. Rev. Lett. **84**, 4521 (2000).

[38] R. Franzosi, V. Penna, and R. Zecchina, Quantum dynamics of coupled bosonic wells within the Bose–Hubbard picture, Int. J. Mod. Phys. B **14**, 943 (2000).

[39] D. Ananikian and T. Bergeman, Gross-Pitaevskii equation for Bose particles in a double-well potential: Two-mode models and beyond, Phys. Rev. A **73**, 013604 (2006).

[40] G. Ferrini, A. Minguzzi, and F. W. J. Hekking, Number squeezing, quantum fluctuations, and oscillations in mesoscopic Bose Josephson junctions, Phys. Rev. A **78**, 023606 (2008).

[41] K. Sakmann, A. I. Streltsov, O. E. Alon, and L. S. Cederbaum, Exact quantum dynamics of a Bosonic Josephson junction, Phys. Rev. Lett. **103**, 220601 (2009).

[42] M. Chuchem, K. Smith-Mannschott, M. Hiller, T. Kottos, A. Vardi, and D. Cohen, Quantum dynamics in the bosonic Josephson junction, Phys. Rev. A **82**, 053617 (2010).

[43] K. Xhani, L. Galantucci, C. F. Barenghi, G. Roati, A. Trombettoni, and N. P. Proukakis, Dynamical phase diagram of ultracold Josephson junctions, New J. Phys. **22**, 123006 (2020).

[44] L. Amico, G. Birkl, M. Boshier, and L.-C. Kwek, Focus on atomtronics-enabled quantum technologies, New J. Phys. **19**, 020201 (2017).

[45] G. Mazzarella, M. Moratti, L. Salasnich, M. Salerno, and F. Toigo, Atomic Josephson junction with two bosonic species, J. Phys. B: At., Mol. Opt. Phys. **42**, 125301 (2009).

[46] F. Lingua, G. Mazzarella, and V. Penna, Delocalization effects, entanglement entropy and spectral collapse of boson mixtures in a double well, J. Phys. B: At., Mol. Opt. Phys. **49**, 205005 (2016).

[47] V. Penna and A. Richaud, Two-species boson mixture on a ring: A group-theoretic approach to the quantum dynamics of low-energy excitations, Phys. Rev. A **96**, 053631 (2017).

[48] A. Richaud, A. Zenesini, and V. Penna, The mixing-demixing phase diagram of ultracold heteronuclear mixtures in a ring trimer, Sci. Rep. **9**, 6908 (2019).

[49] G. Arwas, A. Vardi, and D. Cohen, Superfluidity and chaos in low dimensional circuits, Sci. Rep. **5**, 13433 (2015).

[50] F. S. Cataliotti, S. Burger, C. Fort, P. Maddaloni, F. Minardi, A. Trombettoni, A. Smerzi, and M. Inguscio, Josephson junction arrays with Bose-Einstein condensates, Science **293**, 843 (2001).

[51] M. Albiez, R. Gati, J. Fölling, S. Hunsmann, M. Cristiani, and M. K. Oberthaler, Direct observation of tunneling and nonlinear self-trapping in a single bosonic Josephson junction, Phys. Rev. Lett. **95**, 010402 (2005).

[52] R. Gati and M. K. Oberthaler, A bosonic Josephson junction, J. Phys. B: At., Mol. Opt. Phys. **40**, R61 (2007).

[53] Th. Anker, M. Albiez, R. Gati, S. Hunsmann, B. Eiermann, A. Trombettoni, and M. K. Oberthaler, Nonlinear self-trapping of matter waves in periodic potentials, Phys. Rev. Lett. **94**, 020403 (2005).

[54] G. Spagnolli, G. Semeghini, L. Masi, G. Ferioli, A. Trenkwalder, S. Coop, M. Landini, L. Pezzè, G. Modugno, M. Inguscio, A. Smerzi, and M. Fattori, Crossing over from attractive to repulsive interactions in a tunneling bosonic Josephson junction, Phys. Rev. Lett. **118**, 230403 (2017).

[55] M. Pola, J. Stockhofe, P. Schmelcher, and P. G. Kevrekidis, Vortex–bright-soliton dipoles: Bifurcations, symmetry breaking, and soliton tunneling in a vortex-induced double well, Phys. Rev. A **86**, 053601 (2012).

[56] J.-k. Kim and A. L. Fetter, Dynamics of a single ring of vortices in two-dimensional trapped Bose-Einstein condensates, Phys. Rev. A **70**, 043624 (2004).

[57] L. Pitaevskii and S. Stringari, *Bose-Einstein Condensation and Superfluidity* (Oxford University Press, Oxford, 2016).

[58] C. Barenghi and N. G. Parker, *A Primer on Quantum Fluids* (Springer International Publishing, Cham, 2016).

[59] E. M. Gutierrez, G. A. de Oliveira, K. M. Farias, V. S. Bagnato, and P. C. M. Castilho, Miscibility regimes in a ^{23}Na – ^{39}K quantum mixture, Appl. Sci. **11**, 9099 (2021).

[60] P. C. M. Castilho, E. Pedrozo-Peñafiel, E. M. Gutierrez, P. L. Mazo, G. Roati, K. M. Farias, and V. S. Bagnato, A compact experimental machine for studying tunable Bose–Bose superfluid mixtures, Laser Phys. Lett. **16**, 035501 (2019).

[61] A. Kumar, R. Dubessy, T. Badr, C. De Rossi, M. de Goër de Herve, L. Longchambon, and H. Perrin, Producing superfluid circulation states using phase imprinting, Phys. Rev. A **97**, 043615 (2018).

[62] G. D. Pace, K. Xhani, A. M. Falconi, M. Fedrizzi, N. Grani, D. H. Rajkov, M. Inguscio, F. Scazza, W. J. Kwon, and G. Roati, Imprinting persistent currents in tunable fermionic rings, Phys. Rev. X **12**, 041037 (2022).

[63] T. W. Neely, E. C. Samson, A. S. Bradley, M. J. Davis, and B. P. Anderson, Observation of vortex dipoles in an oblate Bose-Einstein condensate, Phys. Rev. Lett. **104**, 160401 (2010).

[64] K. C. Wright, R. B. Blakestad, C. J. Lobb, W. D. Phillips, and G. K. Campbell, Driving phase slips in a superfluid atom

circuit with a rotating weak link, Phys. Rev. Lett. **110**, 025302 (2013).

[65] W. J. Kwon, G. Del Pace, K. Xhani, L. Galantucci, A. Muzi Falconi, M. Inguscio, F. Scazza, and G. Roati, Sound emission and annihilations in a programmable quantum vortex collider, Nature (London) **600**, 64 (2021).

[66] G. Valtolina, A. Burchianti, A. Amico, E. Neri, K. Xhani, J. A. Seman, A. Trombettoni, A. Smerzi, M. Zaccanti, M. Inguscio, and G. Roati, Josephson effect in fermionic superfluids across the BEC-BCS crossover, Science **350**, 1505 (2015).

[67] W. J. Kwon, G. D. Pace, R. Panza, M. Inguscio, W. Zwerger, M. Zaccanti, F. Scazza, and G. Roati, Strongly correlated superfluid order parameters from dc Josephson supercurrents, Science **369**, 84 (2020).

[68] A. Burchianti, C. Fort, and M. Modugno, Josephson plasma oscillations and the Gross-Pitaevskii equation: Bogoliubov approach versus two-mode model, Phys. Rev. A **95**, 023627 (2017).

[69] R. Franzosi and V. Penna, Chaotic behavior, collective modes, and self-trapping in the dynamics of three coupled Bose-Einstein condensates, Phys. Rev. E **67**, 046227 (2003).

[70] S. Mossmann and C. Jung, Semiclassical approach to Bose-Einstein condensates in a triple well potential, Phys. Rev. A **74**, 033601 (2006).

[71] D. Hernández-Rajkov, N. Grani, F. Scazza, G. D. Pace, W. J. Kwon, M. Inguscio, K. Xhani, C. Fort, M. Modugno, F. Marino, and G. Roati, Connecting shear flow and vortex array instabilities in annular atomic superfluids, Nat. Phys. **20**, 939 (2024).

[72] M. Caldara, A. Richaud, M. Capone, and P. Massignan, Suppression of the superfluid Kelvin-Helmholtz instability due to massive vortex cores, friction and confinement, SciPost Phys. **17**, 076 (2024).

[73] H. C. Prates, D. A. Zezyulin, and V. V. Konotop, Bose-Einstein condensates in quasiperiodic lattices: Bosonic Josephson junction, self-trapping, and multimode dynamics, Phys. Rev. Res. **4**, 033219 (2022).

[74] M. Pigneur and J. Schmiedmayer, Analytical pendulum model for a bosonic Josephson junction, Phys. Rev. A **98**, 063632 (2018).

[75] http://hpc.polito.it.